Title
A Long-Lived Planetesimal Dynamo Powered by Core Crystallization

Journal
Geophysical Research Letters, 48(6)

ISSN
0094-8276

Authors
Maurel, Clara
Bryson, James FJ
Shah, Jay
et al.

Publication Date
2021-03-28

DOI
10.1029/2020gl091917

Peer reviewed

A long-lived planetesimal dynamo powered by core crystallization

Clara Maurel[1], James F. J. Bryson[2], Jay Shah[1], Rajesh V. Chopdekar[3], L. T. Elkins-Tanton[4], C. A. Raymond[5], Benjamin P. Weiss[1]

[1]Department of Earth, Atmospheric, and Planetary Sciences, Massachusetts Institute of Technology, Cambridge, MA, USA.

[2]Department of Earth Sciences, University of Oxford, Oxford, UK.

[3]Advanced Light Source, Lawrence Berkeley National Laboratory, Berkeley, CA, USA.

[4]Arizona State University, Tempe, AZ, USA

[5] Jet Propulsion Laboratory, California Institute of Technology, Pasadena, CA, USA.

Corresponding author: Clara Maurel (cmaurel@mit.edu)

Keywords

Planetesimal, iron meteorites, core crystallization, magnetic field, dynamo

Key Points

- Using IIE iron meteorites, we present the most extended record of dynamo activity on a planetesimal constrained by radiometric dating.
- This extends the epoch of planetesimal dynamo activity to 160 Ma after solar system formation, indicating protracted core crystallization.
- This argues for efficient metal-silicate separation to form a central metallic core with a radius representing >13-20% of the body radius.

Abstract

The existence of numerous iron meteorite groups indicates that some planetesimals underwent melting that led to metal-silicate segregation, sometimes producing metallic cores. Meteorite paleomagnetic records suggest that crystallization of these cores led to the generation of dynamo magnetic fields. Here we describe the magnetic history of the partially differentiated IIE iron meteorite parent body. This is the first planetesimal for which we have a time-resolved paleomagnetic record constrained by $^{40}Ar/^{39}Ar$ chronometry spanning several tens of million years (Ma). We find that the core of the IIE parent body generated a dynamo, likely powered by core crystallization, starting before 78 ± 13 Ma after solar system formation and lasting at least 80 Ma. Such extended core crystallization suggests that the core composed a substantial fraction of the body (≳13-20% core-to-body radius ratio depending on the body's radius), indicating efficient core formation within some partially differentiated planetesimals.

Plain Language Summary

Planetesimals were the first planetary bodies that formed in the solar system, and meteorites are fragments of these planetesimals. Within the first million years of the solar system, some planetesimals melted and formed a metallic core overlain by a rocky mantle. The loss of heat and release of buoyant fluids generated through the crystallization of these cores could have caused the residual liquid to churn, creating a magnetic field by the dynamo effect. Some meteorites contain minerals that align their magnetic moments with such magnetic fields, analogous to a compass needle in Earth's field. Even though the ancient field disappeared billions of years ago, this alignment can still be retained by meteorites today. Because core solidification and generation of magnetic fields are intrinsically related, the magnetic record of meteorites is a powerful proxy for investigating the solidification and thermal history of planetesimals. Here, we present a time-resolved record captured by three meteorites from the same parent planetesimal of a magnetic field powered by the solidification of their parent planetesimal's core. It is the most extended record of such fields for which we have absolute ages, and this record supports the hypothesis that some planetesimals efficiently melted and formed significantly large metallic cores.

1 Introduction

Planetesimals were the first generation of 1- to 1000-km diameter planetary bodies to form in the solar system and are key intermediate stages in planet formation. Due to heating by the decay of the short-lived radioactive isotope ^{26}Al [*Hevey and Sanders*, 2006], percolation of Fe-Ni melts variably enriched in sulfur and other light elements initiated differentiation and the formation of metallic cores in a number of planetesimals [*Terasaki et al.*, 2008]. Some of these bodies, however, appear to have been only partially differentiated (i.e., simultaneously and durably contained chondritic and achondritic material; *Elkins-Tanton et al.*, 2011; *Weiss and Elkins-Tanton*, 2013). The internal structures and modes of formation of partially-differentiated planetesimals remain to be completely understood despite longstanding interest [*Urey*, 1959; *Fish et al.*, 1960; *Lovering*, 1962; *Wasserburg et al.*, 1968]. Melting experiments and simulations show that metal percolation is efficient once the volume melt fraction in a metal-silicate mixture exceeds ~2% [*Terasaki et al.*, 2008; *Ghanbarzadeh et al.*, 2017]. Partially differentiated bodies could therefore have formed a differentiated interior while preserving or accumulating a chondritic crust [*Elkins-Tanton et al.*, 2011; *Sahijpal and Gupta*, 2011; *Weiss and Elkins-Tanton*, 2013; *Neumann et al.*, 2018]. Alternatively, they could have consisted of patchworks of localized differentiation products resulting from late and incomplete melting [*Hunt et al.*, 2018].

A discriminating factor between a differentiated interior overlain by a chondritic crust and a patchwork of localized differentiation products is the existence of a sizeable metallic core. One approach to constrain the presence and size of a core is to search for evidence of its putative magnetic activity recorded as remanent magnetization in mantle material. For instance, meteorite remanent magnetization has been used to argue that a number of parent bodies generated magnetic fields through dynamo activity (i.e., powered by advection of molten metal) [*Weiss et al.*, 2010]. Purely thermally-driven advection can occur as long as the heat flux across the core-mantle boundary (CMB) remains larger than the adiabatic heat flux within the core. On planetesimals, this mechanism could have persisted up to ~20 Ma after CAI-formation [*Elkins-Tanton et al.*, 2011; *Bryson et al.*, 2019b]. Dynamo activity could also have been powered by core solidification, potentially either by the release of light elements into the remaining liquid if solidification occurred outwardly, or by "iron snow" and/or the delamination of a solid layer forming at the CMB if solidification occurred inwardly [*Chabot and Haack*, 2006; *Nimmo*, 2009; *Williams*, 2009; *Rückriemen et al.*, 2015; *Neufeld et al.*, 2019]. The duration of such compositional dynamos

ultimately depends on the size of the core and direction of solidification. As such, one can potentially constrain the core size by measuring time-resolved paleomagnetic records using multiple meteorites from the same parent body, which place bounds on the duration of the magnetic activity.

Compositionally-driven dynamos have been proposed to explain the natural remanent magnetization (NRM) of five main-group pallasites, one L/LL chondrite, one IVA iron, one H chondrite and two silicate-bearing IIE iron meteorites [*Tarduno et al.*, 2012; *Bryson et al.*, 2015; *Nichols et al.*, 2016; *Bryson et al.*, 2017; *Nichols*, 2017; *Shah et al.*, 2017; *Bryson et al.*, 2019a; *Maurel et al.*, 2020]. Timing for compositional dynamo activity has been proposed for the main-group pallasites parent body [*Tarduno et al.*, 2012; *Bryson et al.*, 2015; *Nichols et al.*, 2016]. However, the times in this record were estimated by combining the meteorites' measured cooling rates at 500°C with numerical simulations of conductive planetesimal cooling rather than being recovered from radiometric dating. It is therefore dependent on model parameters such as the size of the body, its thermal conductivity as a function of depth, and the assumed cooling mechanism (convective or conductive).

Based on a variety of petrographic, geochemical and magnetic data, the parent body of the silicate-bearing IIE iron meteorites has been described as a partially-differentiated planetesimal, composed of chondritic and achondritic material [*Ruzicka*, 2014; *Kruijer and Kleine*, 2019; *Maurel et al.*, 2020]. A number of internal structures have been proposed for this parent body: a partially molten body with an incipient core catastrophically disrupted to form small IIE secondary bodies [*Ruzicka*, 2014]; a body with a differentiated interior overlain by a chondritic layer impacted to form one or several IIE reservoirs [*Maurel et al.*, 2020]; and a body that experienced localized differentiation due to late and incomplete melting [*Kruijer and Kleine*, 2019].

Here, we build upon a recent paleomagnetic study of the IIE irons Techado and Colomera [*Maurel et al.*, 2020] and measure the remanence carried by the IIE iron Miles. We combine the $^{40}Ar/^{39}Ar$ age of the three meteorites with their magnetic records to constrain potential existence of a sizeable core, the temporal evolution of its dynamo, and the onset and duration of its crystallization. We estimate a minimum core-to-body ratio for the IIE parent body and use this to constrain the possible internal structures of partially-differentiated bodies.

2 Formation and magnetic mineralogy of IIE iron meteorites

In the scenarios proposed to explain the nature of the IIE parent body (Section 1), the IIE irons form through one or several impacts that mixed silicates and metal together without catastrophically disrupting the body within the first few tens of Ma after CAI formation [*Ruzicka*, 2014; *Kruijer and Kleine*, 2019; *Maurel et al.*, 2020]. We note, however, that the idea that the body was disrupted and reaccreted during such impacts cannot be ruled out. Buoyancy-driven segregation of the molten metal-silicate mixture would have been prevented by exposure to near-surface temperatures and rapid cooling (> 2.5°C h^{-1} at 850–1000°C as indicated by the presence of silicate glass; *Ruzicka*, 2014). Following the impact, the source regions for the meteorites would have been buried under tens of km of material [*Maurel et al.*, 2020] to explain the presence of metallographic microstructures that form at slow cooling rates (<10,000 °C Ma^{-1} below ~600°C) [*Ruzicka*, 2014].

Slow cooling enabled the formation of cloudy zones (CZs), nanoscale intergrowths of Ni-rich ferromagnetic islands embedded in a Ni-poor paramagnetic matrix [*Yang et al.*, 1996; *Blukis et al.*, 2017]. CZs form by spinodal decomposition of taenite with composition ranging from ~41–30 wt.% Ni, and are separated from the ~5 wt.% Ni kamacite by a μm-thick rim with ≳48 wt.% Ni (Fig. S1). The rim and adjacent CZ islands are initially composed of taenite, which upon slow cooling (≲5,000 °C Ma^{-1}) through 320°C undergoes crystallographic ordering and forms tetrataenite. The resulting increase in magnetocrystalline anisotropy causes the magnetic state of CZ islands to change from that of a vortex to two domains [*Einsle et al.*, 2018]. The tetrataenite rim, on the other hand, remains in the magnetic multidomain state due to its larger size. Recent micromagnetic simulations suggest that the combination of an external magnetic field and magnetostatic interactions between islands subsequently de-nucleates the domain wall in these islands, forming an ensemble of single-domain islands with average magnetization biased toward the external field direction [*Einsle et al.*, 2018; *Yeem and Harrison*, 2019]. At this point, any prior NRM that may have been acquired by the parent taenite phase in CZ islands is replaced by the NRM of tetrataenite without apparent inheritance [*Einsle et al.*, 2018]. Single-domain tetrataenite CZ islands, with a magnetic coercivity > 1 T [*Uehara et al.*, 2011], can preserve their NRM over the age of the solar system.

It was previously shown that Techado and Colomera cooled through ~350°C at 4.6 ± 1.9 and 2.5 ± 1.4°C Ma^{-1}, respectively [*Maurel et al.*, 2020]. By comparing a cloudy zone formation model [*Maurel et al.*, 2019] to the average island size and Ni content in a given region of the CZ

(supplementary text S1–S2), we estimate that Miles cooled through this temperature at 3.8 ± 2.6°C Ma^{-1}. At these cooling rates, the Ar closure temperature of the 0.1–1-mm feldspar grains, the dominant Ar-bearing phase in Miles, is 330 ± 70°C [*Cassata et al.*, 2011]. This temperature range overlaps the tetrataenite formation temperature, indicating that the $^{40}Ar/^{39}Ar$ age of the meteorites can be used to approximately date when their CZs were magnetized.

The fact that Techado's and Colomera's CZs recorded magnetic activity around their $^{40}Ar/^{39}Ar$ ages of 78 ± 13 and 97 ± 10 Ma after CAI-formation [*Bogard et al.*, 2000] was interpreted as evidence that the IIE parent body generated a compositionally-driven dynamo [*Maurel et al.*, 2020]. The late timing of this activity rules out early field sources such as the solar nebula [*Wang et al.*, 2017] or a thermally-driven dynamo [*Elkins-Tanton et al.*, 2011; *Bryson et al.*, 2019b], while the long duration over which tetrataenite acquired its magnetization rule out transient or quickly time-varying sources such as impact-generated plasma fields [*Hood and Artemieva*, 2008], core mechanical stirring by impacts [*Le Bars et al.*, 2011], or the solar wind [*Oran et al.*, 2018]. It also implies that the field must have been directionally stable over the period of magnetization acquisition. A crustal field, resulting from the magnetization of an H-chondrite-like crust acquired during earlier magnetic activity of the parent body would also have been orders of magnitude too weak to explain the results obtained [*Maurel et al.*, 2020]. With an $^{40}Ar/^{39}Ar$ age of 159 ± 9 Ma after CAI-formation [*Bogard et al.*, 2000], Miles has the potential to extend the known paleomagnetic record for the IIE body by > 60 Ma.

3 Experimental method

Our measurements followed the experimental method of *Bryson et al.* (2019a) and *Maurel et al.* (2020). A 3×6×1-mm sample of Miles from the Harvard Museum of Natural History collection was polished manually down to 0.3 μm. We selected two areas located ~1 mm apart, encompassing kamacite, tetrataenite rim and CZ (hereafter called K–T interfaces; supplementary Figs. S2-S3). To measure the three components of remanent magnetization at the sub-micrometer scale, we used three-axis X-ray photoemission electron microscopy (XPEEM) performed at beamline 11.0.1.1 at the Advanced Light Source (Berkeley, CA). The original experimental protocol of this technique only yielded one component of magnetization [*Bryson et al.*, 2015; *Nichols et al.*, 2016; *Bryson et al.*, 2017; *Nichols et al.*, 2018], but it was recently improved to enable all three components to be recovered, providing more accurate relative paleodirections [*Bryson et al.*, 2019a; *Maurel et al.*,

2020]. The sample was first Ar-sputtered for a total of 15 hours to remove surface damage caused by polishing. XPEEM images were then collected with a 10-µm field-of-view along 260 and 290 µm of K–T interface 1 and 2, respectively (supplementary Fig. S3). At each location, four images were acquired with alternating right- and left-circularly polarized X-rays, first tuned to the Fe L_3 absorption edge (707.4 eV; Fig. 1a) and then off-edge (702 eV). The operation was repeated four times to average identical images and minimize the effect of high-frequency noise. After data were collected on both K–T interfaces, the sample was rotated ~120° around its surface normal twice (Fig. 1b,c), with the same measurement sequence repeated each time.

For each on-edge image, the following pixel-by-pixel operation was first conducted to remove both the background intensity caused by non-resonant X-ray absorption from atoms other than Fe and the effect of surface topography from the signal:

$$I^{\pm}_{\mathrm{corr}} = \left(I^{\pm}_{\mathrm{on-edge}} - I^{\pm}_{\mathrm{off-edge}}\right)/I^{\pm}_{\mathrm{off-edge}} \quad (1)$$

where $I^{\pm}_{\mathrm{on-edge}}$ and $I^{\pm}_{\mathrm{off-edge}}$ are the pixel intensities of the corresponding on-edge and off-edge images for each polarization; + and – refer to the right- and left-circular beam polarization directions. The X-ray flux absorbed by the sample depends on the angle between the local surface magnetization and the helicity of the X-ray. This introduces a contrast between images collected with right- and left-circularly polarized X-rays called X-ray magnetic circular dichroism (XMCD; *Stöhr et al.*, 1993). XMCD contrast maps, whose intensity (I_{XMCD}) depends on the direction of the surface magnetization relative to the X-ray beam direction, are calculated from corrected XPEEM images ($I^{\pm}_{\mathrm{corr}}$):

$$I_{\mathrm{XMCD}} = (I^{-}_{\mathrm{corr}} - I^{+}_{\mathrm{corr}})/(I^{-}_{\mathrm{corr}} + I^{+}_{\mathrm{corr}}) \quad (2)$$

The six possible magnetization directions of tetrataenite, oriented along the <100> directions of the parent taenite phase, correspond to six quantized values of I_{XMCD} (three positive/negative values corresponding to the positive/negative vector projections onto the X-ray beam; Fig. 1d–f). These six values are visible within the homogenous µm-sized domains in the tetrataenite rim. The CZ islands, which have the same crystallographic orientation as the rim, also adopt one of these six magnetization directions during tetrataenite formation. However, because Miles' CZ islands

(≲110-nm; supplementary text S1) are not readily distinguishable in XMCD images due to insufficient spatial resolution, we used the rim to determine the six possible XMCD values of the six possible magnetization directions for each image and each sample rotation.

To estimate the three components of the paleofield from the XMCD maps acquired along each K–T interface, we combined 1) the six XMCD values measured from the tetrataenite rim and 2) the average XMCD value within each 0.5×9-µm region-of-interest in the CZ (Fig. 1d), under the assumption that the islands' magnetization directions follow a Maxwell-Boltzmann distribution [*Bryson et al.*, 2014]:

$$I^{j}_{\mathrm{XMCD,CZ}} = \frac{\sum_{i=1}^{i=6} I^{j}_{\mathrm{XMCD},i} \exp(\alpha B_i)}{\sum_{i=1}^{i=6} \exp(\alpha B_i)} \quad (3)$$

where j = R1:R3 denote the sample rotation, i = 1:6 denote the six possible magnetization directions ($\pm x, \pm y$ and $\pm z$), B_i are the components of the ancient external field in these directions, $I^{j}_{\mathrm{XMCD},i}$ are the XMCD intensities for each direction collected in the tetrataenite rim for one sample rotation and $I^{j}_{\mathrm{XMCD,CZ}}$ is the XMCD intensity of the region of interest in the CZ. We also have $\alpha = M_s V / k_B T$, where M_s is the saturation magnetization of tetrataenite (1300 kA m^{-1}), k_B is the Boltzmann constant and V is the volume of the islands at T = 320°C, the tetrataenite formation temperature. Using a numerical model of CZ formation, and the local Ni content of the CZ regions of interest (supplementary text S1), we estimate that islands were ~78% of their present-day size at 320°C (supplementary text S2; *Maurel et al.*, 2019). The Maxwell-Boltzmann assumption does not account for the magnetostatic interactions that exist between islands [*Einsle et al.*, 2018] and introduces an uncertainty in the paleointensity estimates (see Section 4). With the XMCD intensities collected for the three sample rotations, eq. (3) becomes a system of three equations that can be solved for B_x, B_y, B_z.

4 Results

Solving eq. (3), we calculated the paleodirections for each region-of-interest selected in the two CZs. Each K–T interfaces was analyzed using electron backscattered diffraction in order to mutually orient the paleodirections in a known reference frame (supplementary text S3;

supplementary Fig. S5). We found that both sets of directions are biased (supplementary text S4a), indicating that each CZ likely formed in the presence of a paleofield with substantial intensity. This result is supported by Watson's test for randomness [*Watson*, 1956] showing that the paleodirections are not drawn from a uniform distribution (supplementary text S4b). Using the V_w statistic [*Watson*, 1983], we also cannot reject at 95% confidence the hypothesis that both K–T interfaces exhibit a common average paleodirection (Fig. 1g, supplementary text S4b). These observations indicate that Miles cooled in the presence of a magnetic field sufficiently strong to impart a resolvable bias in CZ island magnetization directions, as previously interpreted for Techado and Colomera [*Maurel et al.*, 2020]. Using eq. (3), we also calculated the magnitude of the vector (B_x, B_y, B_z) and estimated a paleointensity of 32 ± 15 μT and 34 ± 11 μT (2 s.e.) for K–T interface 1 and 2, respectively.

The uncertainties on the relative paleodirections (Fig. 1g) and paleointensities were estimated considering the measurement noise (due to time-dependent drifts of the X-ray beam and the varying resolution of the instrument's electron optics) and the counting statistical uncertainties associated with the limited number of islands included in each XPEEM dataset (supplementary text S4c). Two additional sources of uncertainty were also considered.

First, the spatial arrangement of single domain islands in the CZ causes magnetostatic interactions [*Blukis et al.*, 2020] that influence the paleointensity and paleodirection. These interactions are intrinsic to one CZ and do not influence other spatially distinct CZs. Given that we recover similar paleodirections from both CZs, we estimate that these interactions have a minor effect on paleodirection. However, like in almost any closely-packed configuration of single domain grains, interactions will typically yield an underestimation of the paleointensity [*Dunlop and Özdemir*, 1997], possibly by up to an order of magnitude [*Harrison and Lascu*, 2014].

Second, the IIE irons most likely cooled in a metallic reservoir, where dominant low-coercivity kamacite grains could add an induced component to the field experienced by the CZs. The induced field would likely be spatially homogenous across the two CZs analyzed and therefore not affect the relative paleodirection uncertainty; it could, however, yield an overestimation of the paleointensity by a factor of ~3 [*Maurel et al.*, 2020]. The field produced by another metallic reservoir that acquired a remanent magnetization earlier in time would be unlikely to magnetize the three IIE irons given the decay of field intensity with distance. We note that the multidomain kamacite surrounding the CZs could acquire a thermoremanent magnetization at ~780°C. We do

not know whether the remanent field of the kamacite could be responsible for the magnetization of the CZ, and therefore cannot rule out this possibility. However, it would not invalidate the fact that the IIE parent body generated a dynamo field but rather shift backward the time of the record.

Accounting for the quantifiable uncertainties, the paleointensity recorded by Miles could range from 10 to 300 μT, indistinguishable from paleointensity ranges estimated for Techado (10–360 μT) and Colomera (5–150 μT) [*Maurel et al.*, 2020]. As for Techado and Colomera, the relatively high paleointensity, young age and long duration of CZ NRM acquisition indicate that Miles also most likely recorded a dynamo-generated magnetic field powered by core crystallization on its parent body. The magnetic records of the three meteorites indicate that the dynamo was active on the IIE parent body for >80 Ma, initiating before 78 ± 13 and lasting until at least 159 ± 9 Ma after CAI-formation. This is the most extended radiometrically-dated record of a planetesimal's dynamo activity to date (Fig. 2).

5 Discussion

5.1 Evidence for late geological activity on planetesimals

Our results indicate that the crystallization of the IIE parent body's core lasted at least until Miles recorded its NRM, which implies that the IIE parent planetesimal contained a partially liquid, advecting metallic core until > 159 ± 9 Ma after CAI-formation. In comparison, existing $^{108}Pd/^{109}Ag$ model ages (which date when iron meteorites cooled through 700-500°C; e.g., *Matthes et al.,* 2020) suggest that some meteorites from the IIAB, IID and IIIAB iron groups crystallized by 11 Ma after CAI-formation [*Matthes et al.*, 2015; 2020]. For the IIIAB irons, where the greatest number of samples have been analyzed (four meteorites), these ages were interpreted as evidence for early core excavation by collisions [*Matthes et al.*, 2020]. On the other hand, our results support recent numerical studies of planetesimal thermal evolution arguing for long-lived molten cores up to several hundred Ma after CAI formation in objects that largely retained their mantles (e.g., *Bryson et al.*, 2019b). For example, Vesta's core has been predicted to have remained partially liquid up to or beyond ~200 Ma after CAI formation [*Neumann et al.*, 2014]. Importantly, these types of numerical studies are also able to reproduce short core solidification timescales akin to that recovered from $^{108}Pd/^{109}Ag$ ages for parent bodies that experienced core-excavation events [*Neufeld et al.*, 2019].

5.2 Constraints on the size of the IIE parent body

The fact that core crystallization on the IIE parent body lasted at least until 159 ± 9 Ma after CAI-formation can provide a lower limit on the size of the body. *Bryson et al.* (2019b) used a one-dimensional approach to model the convective and conductive cooling of planetesimals with differentiated interiors and chondritic crusts. This two-stage accretion model varied the time of accretion between 0 and 4.5 Ma after CAI-formation and the size of the simulated objects from 20 to 500-km radius; core-to-body radius ratio ranged from 2 to 50% (upper limit imposed in the simulations), and the thickness of the unmelted layer from 0 to 94% of the body's radius. As an upper limit on the end of core crystallization, this study reported the time when the core reached the FeS eutectic temperature (~988°C; e.g., *Buono and Walker*, 2011) and the total latent heat of crystallization was extracted from the core. Among the aforementioned parameters (i.e., accretion time, final body radius, core-to-body ratio, thickness of chondritic layer), the end of crystallization is controlled predominantly by the body radius [*Bryson et al.*, 2019b]. These simulations do not account for impact event(s) akin to the IIE-forming event(s). However, given that these event(s) most likely occurred tens of Ma before the epoch investigated here, we assume that temperatures would have re-equilibrated to produce a regular temperature gradient with depth throughout the body.

According to this model, the IIE parent body would have been ≳ 220-km in radius for its core to have entirely solidified later than 159 ± 9 Ma after CAI-formation (Fig. 3). Moreover, this model suggests that Techado, Colomera and Miles cooled at depths ranging from ~30 and ~80 km (supplementary text S5). We explored whether regolith, with a thermal diffusivity two orders of magnitude smaller than chondritic material [*Haack et al.*, 1990], could delay appreciably the end of crystallization. However, a regolith layer akin to that of the asteroid Vesta (on average ~1 km; *Denevi et al.*, 2016) added after accretion only delays the end time of crystallization by 0.75 Ma (supplementary text S6), which is negligible given the other uncertainties of the model, such as the discrete accretion scenario and the treatment of the CMB heat flux [*Bryson et al.*, 2019b].

The fact that the core must have started to crystallize prior to 78 ± 13 Ma after CAI formation does not readily translate into an upper size limit due to the uncertainty in the concentration and action of sulfur in planetesimal cores. Nonetheless, using core thermal profiles simulated with the model of *Bryson et al.* (2019b), we can roughly estimate that with a core S content of ≲ 26 wt.%, a planetesimal as large as 500 km in radius could have reached FeS solidus

earlier than Techado's $^{40}Ar/^{39}Ar$ age (supplementary text S7). This is in agreement with S contents of $\lesssim$ 20 wt.% estimated from compositional measurements of iron meteorites [*Goldstein et al.*, 2009]. It is worth noting that the collisional lifetime of such large planetesimal exceeds the age of the solar system [*Bottke et al.*, 2005]. Unless it was at some point ejected from the solar system, the IIE parent body is not likely to have been as large as 500 km in radius.

5.3 Internal structure of the IIE parent body

To constrain the core-to-body radius ratio for the IIE parent body, we compared our data to the simulations conducted for different values of this ratio by *Bryson et al.* (2019b). For a planetesimal radius < 250 km, 90% of simulations have the core of the IIE parent body being $\gtrsim$19% of the body's total radius (>0.7 vol.%) for complete core crystallization to have occurred later than 159 ± 9 Ma after CAI-formation (Fig. 3). This decreases to $\gtrsim$14 and $\gtrsim$13% if we include planetesimals up to 350 and 450 km in radius, respectively. The lower limits on the core-to-body radius ratios are consistently smaller than the core sizes estimated from the metal content of ordinary chondrites (~43%, ~34% and ~27% radius ration for H, L and LL chondrites, respectively; Fig. 3) calculated assuming complete differentiation [*Krot et al.*, 2014]. The presence of an H-chondrite-like silicate crust—based on the isotopic and compositional affinity between IIE silicates and H chondrites—restricts the core-to-body radius ratio to <43%. These observations are consistent with the core-to-body radius ratio of Vesta (~41–43%), the only core size inferred directly from both bulk density measurements and geochemical constraints [*Russell et al.*, 2012].

Our magnetic data provide further evidence that core formation within partially-differentiated planetesimals could have been an efficient process. The existence of a substantial core requires significant melting of the IIE parent body. This matches well with the proposed scenario whereby partially differentiated bodies formed by protracted or incremental accretion of chondritic material onto a differentiated planetesimal seed [*Sahijpal and Gupta*, 2011]. It is also consistent with a scenario similar to that proposed for the acapulcoite-lodranite parent body, where a thin chondritic crust is preserved despite the formation of a significant metallic core after a short period of accretion [*Neumann et al.*, 2018]. On the other hand, although our results do not exclude IIE metal having formed by partial melting in a yet chondritic crust [*Kruijer and Kleine*, 2019], they still require that the deep interior of the planetesimal was differentiated. This contrasts with the scenario of localized melting without formation of a substantial core proposed for some of the

IAB iron meteorite parent bodies [*Worsham et al.*, 2017; *Hunt et al.*, 2018]. In agreement with this scenario, XPEEM data collected on three IAB irons (main-group, sLL and sLH) show that their parent bodies most likely did not generate a magnetic field at the time of tetrataenite formation [*Bryson et al.*, 2014; *Nichols et al.*, 2018]. This supports the idea that multiple mechanisms may have led to the formation of partially differentiated planetesimals.

6 Conclusion

The silicate-bearing IIE iron meteorites likely formed through one or several impact events that created reservoirs of mixed metal and silicates on a partially-differentiated planetesimal. The IIE irons Techado, Colomera and Miles cooled in a magnetic field of order of ~5–360 μT between 78 ± 13 and 159 ± 9 Ma after CAI-formation, most likely generated by compositional dynamo activity on their parent body. This is the most extended radiometrically-dated record of dynamo activity on a planetesimal collected to date. This implies that the crystallization of the IIE parent body's core lasted >80 Ma and was ongoing 159 ± 9 Ma after CAI-formation. These observations indicate that this planetesimal likely was at least ~220 km in radius and had a core-to-body radius ratio >13-19% depending on its size. The fact that this planetesimal was partially differentiated restricts the core-to-body radius ratio to <43 %. Together, these findings require efficient metal-silicate segregation and significant melting of the interior of the IIE parent body, achievable with both a protracted or incremental accretion of cold material onto a differentiated planetesimal, or faster accretion with only partial melting. By comparison, it refutes the hypothesis that the IIE parent body was only composed of metal veins and pools without significant metal segregation and core formation. The determination of $^{40}Ar/^{39}Ar$ ages for unstudied IIE irons could potentially reveal meteorites older than 4,489 Ma (i.e., than Techado), or up to a few hundred Ma younger than 4,408 Ma (i.e., than Miles). This could provide the opportunity to probe the onset or decay of this planetesimal's dynamo activity.

Acknowledgments, Samples, and Data

We thank the Harvard Museum of Natural History for the loan of Miles. We thank C. I. O. Nichols for helpful discussions. This research used the Advanced Light Source, a Department of Energy Office of Science User Facility (contract DE-AC02-05CH11231). We thank two anonymous reviewers for their valuable comments, and M. Korte for the editorial handling. C. M. and B. P. W. thank the NASA Discovery Program (contract NNM16AA09C), the NASA Emerging Worlds program (grant NNX15AH72G) and T. F. Peterson, Jr. for support. C. M. and B. P. W. conceived the project. C. M., J. F. J. B. and J. S. conducted the XPEEM experiments. R. V. C. assisted with the XPEEM data acquisition. C. M. analyzed the paleomagnetic data and conducted the SEM-EDS measurements. J. F. J. B. developed the thermal evolution model and conducted the simulations. C. A. R. and L. T. E.-T. contributed to the discussions of the implications of the results. B. P. W. supervised the project. All authors were involved in writing the manuscript. Authors declare no competing interests. All data needed to evaluate the conclusions in the paper are present in the paper or the supporting information. The raw XPEEM data collected for this work can be found on the Magnetics Information Consortium (MagIC) database at https://www.earthref.org/MagIC/16862 (DOI: 10.7288/V4/MAGIC/16862).

Figures

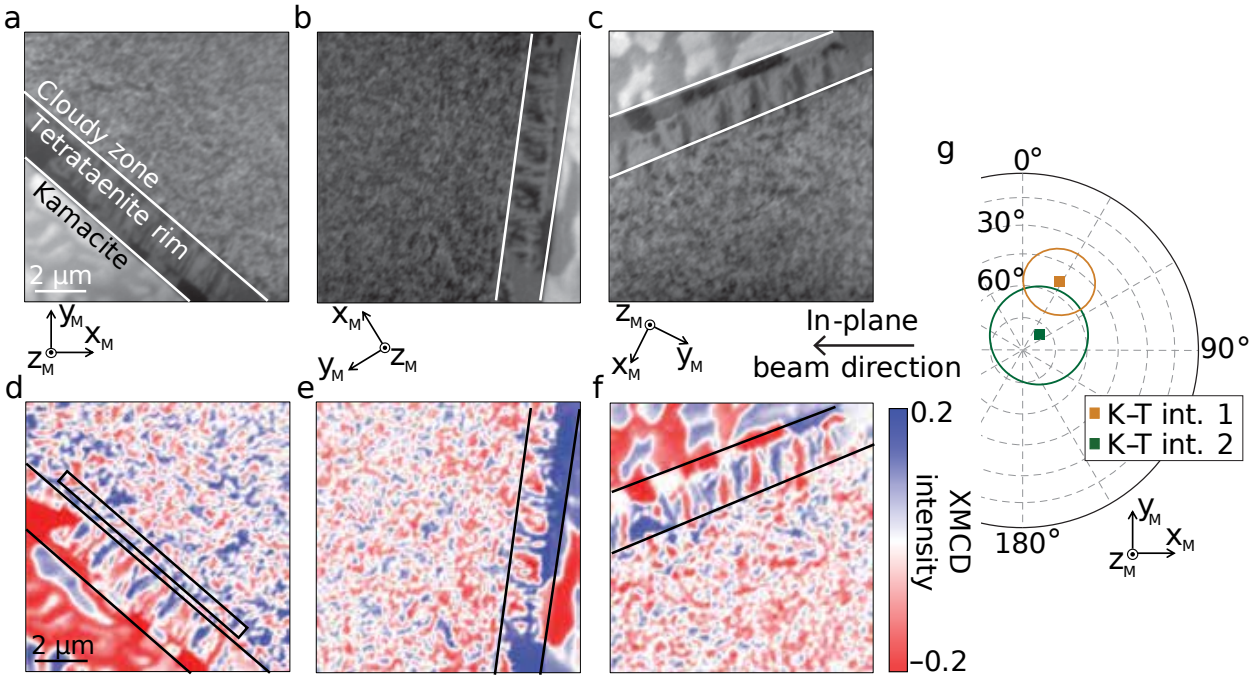

Fig. 1. (**a–c**) XPEEM images of one location along K–T interface 1 (supplementary Fig. S2). These images were obtained with right-circularly polarized X-rays at 707.2 eV (Fe L_3 absorption edge) for three different in-plane rotations of ~120° of the sample. The grey scale quantifies the relative flux of electron captured in the optics. The in-plane azimuth of the beam is shown; it arrives at 30° out of the plane of the image. (**d–f**) Corresponding XMCD contrast maps. A typical region-of-interest in the CZ is shown by a rectangle on panel (d). The tetrataenite rim is marked by the black lines. (**g**) Equal area projection showing the average relative direction of the paleofield estimated from the two K–T interfaces analyzed in Miles. Ellipses show the 95% confidence intervals accounting for the measurement uncertainty and counting statistical uncertainty. The reference frame refers to that of supplementary Fig. S2.

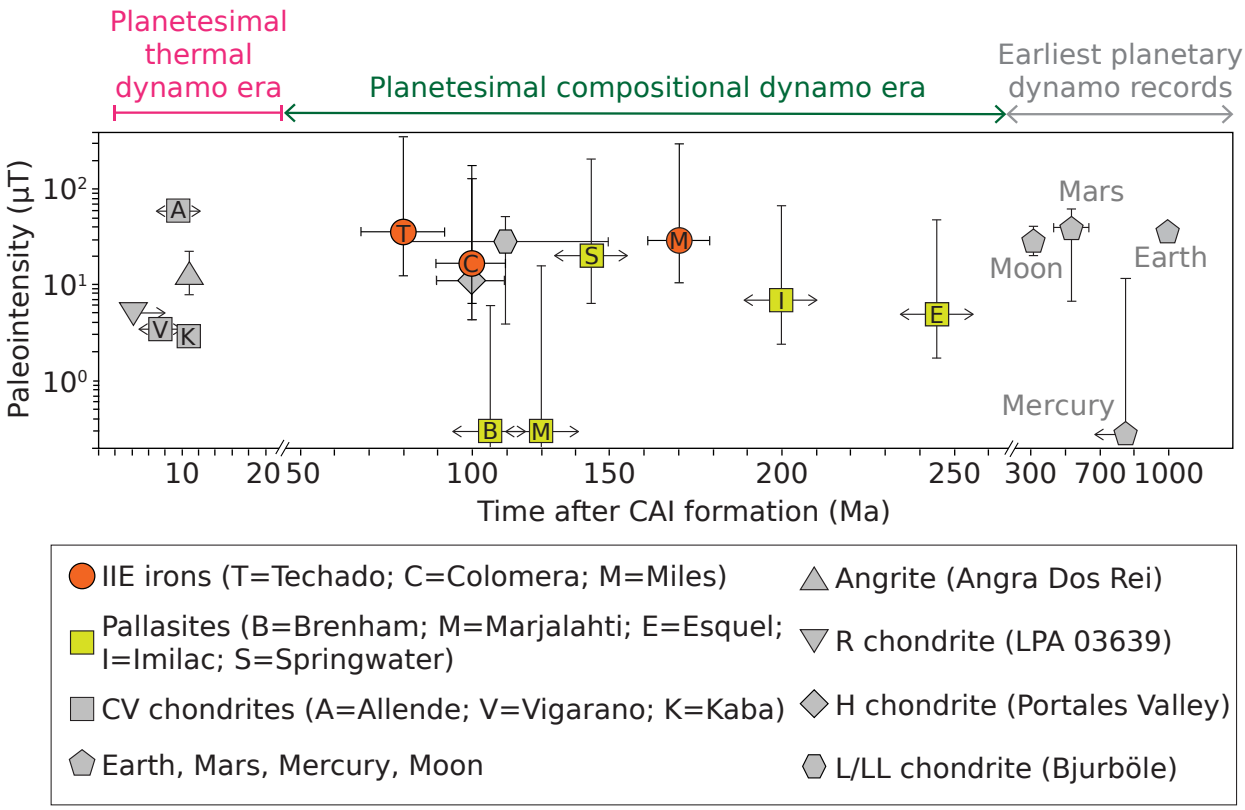

Fig. 2. Summary of the field intensities estimated from meteorite paleomagnetic measurements for different parent bodies as a function of time after CAI-formation. All records shown have been attributed to dynamo activity. Before ~20 Ma after CAI-formation, the dynamo could be powered by thermal convection for parent bodies ≳ 100-km radius [*Elkins-Tanton et al.*, 2011; *Bryson et al.*, 2019b]. Later than 50 Ma after CAI-formation, it is most likely that the dynamo activity was driven by core crystallization [*Bryson et al.*, 2019b], although the boundaries of this era are uncertain. Planetesimals that underwent early mantle-stripping events could have generated a compositional dynamo within the first 20 Ma after CAI formation (e.g., *Neufeld et al.*, 2019). The oldest magnetic records for terrestrial planets are shown for reference: planetesimals powered the earliest planetary magnetic activity in the solar system. Left (right) arrows indicate upper (lower) limits. The timing of the pallasite records is based on conductive cooling simulations assuming a fully-differentiated 200-km radius parent body and so is dependent on model parameters as indicated by the arrows. Data from [*Weiss et al.*, 2002; 2008; *Tarduno et al.*, 2010; *Carporzen et al.*, 2011; *Biggin et al.*, 2015; *Bryson et al.*, 2015; *Johnson et al.*, 2015; *Gattacceca et al.*, 2016; *Nichols et al.*, 2016; *Garrick-Bethell et al.*, 2017; *Nichols*, 2017; *Shah et al.*, 2017; *Wang et al.*, 2017; *Bryson et al.*, 2019a; *Maurel et al.*, 2020].

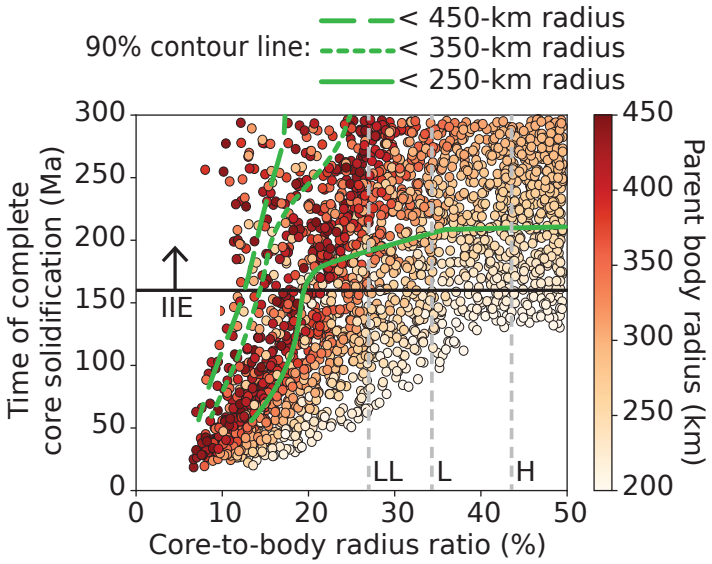

Fig. 3. Time of complete core solidification as a function of core-to-body radius ratio for partially- to fully-differentiated planetesimals with final radii between 200 and 450 km. Points represent the outcomes of cooling models conducted by *Bryson et al.* (2019b) for a wide range of accretion times and thickness of added chondritic material. The color bar indicates the final radius of the planetesimal. The time of solidification is an absolute upper limit, as it represents the time when the planetesimal reached the FeS eutectic temperature and all the latent heat of crystallization was extracted from the core. The horizontal black line shows the youngest time for complete solidification of the IIE parent body core recovered from the magnetic record of Miles. The three green lines mark the 90% contours for parent bodies with radius smaller than 250, 350 and 450 km. If we only consider parent bodies up to 250 km in radius, 90% of the simulations that produce the end of core solidification after 160 Ma after CAI formation have core-to-body radius ratios >19%. This minimum ratio becomes 14% and 13% when including bodies up to 350 and 450 km in radius, respectively. The three gray vertical dashed lines show the core-to-body radius ratios calculated from the metal abundances of H, L and LL chondrites [*Krot et al.*, 2014] under the assumption that all the metal enters the core if bodies made of these meteorites were to differentiate.

References

Berndt, T., Muxworthy, A. R. & Fabian, K. (2016). Does size matter? Statistical limits of paleomagnetic field reconstruction from small rock specimens, *J. Geophys. Res.*, *121*, 15–26, doi:10.1002/2015JB012441

Biggin, A. J., Piispa, E. J., Pesonen, L. J., Holme, R., Paterson, G. A., Veikkolainen, T. & Tauxe L. (2015). Palaeomagnetic field intensity variations suggest Mesoproterozoic inner-core nucleation, *Nature*, *526*, 245–248, doi:10.1038/nature15523

Blukis, R., Pfau, B., Günther, C. M., Hessing, P., Eisebitt, S. , Einsle, J. & Harrison, R. J. (2020). Nanoscale imaging of high-field magnetic hysteresis in meteoritic metal using X-ray holography, *Geochem. Geophys. Geosyst.*, *21*, e09044, doi:10.1029/2020GC009044

Blukis, R., Rüffer, R., Chumakov, A. I. & Harrison R. J. (2017). A high spatial resolution synchrotron Mössbauer study of the Tazewell IIICD and Esquel pallasite meteorites, *Meteorit. Planet. Sci., 52*, 925–936, doi:10.1111/maps.12841

Bogard, D. D., Garrison, D. H. & McCoy, T. J. (2000). Chronology and petrology of silicates from IIE iron meteorites: evidence of a complex parent body evolution, *Geochim. Cosmochim. Acta*, *64*, 2133–2154, doi:10.1016/S0016-7037(00)00355-0

Bottke, W. F., Durda, D. D., Nesvorný, D., Jedicke, R., Morbidelli, A., Vokrouhlický, D. & Levison, H. F. (2005). The fossilized size distribution of the main asteroid belt, *Icarus*, *175*, 111–140, doi:10.1016/j.icarus.2004.10.026

Bryson, J. F. J., Weiss, B. P., Getzin,, B. Abrahams, J. N. H., Nimmo, F. & Scholl, A. (2019a). Paleomagnetic evidence for a partially differentiated ordinary chondrite parent asteroid, *J. Geophys. Res.*, *69*, 972–19, doi:10.1029/2019JE005951

Bryson, J. F. J., Weiss, B. P., Harrison, R. J., Herrero-Albillos, J. & Kronast, F. (2017). Paleomagnetic evidence for dynamo activity driven by inward crystallisation of a metallic asteroid, *Earth Planet. Sci. Lett.*, *472*, 152–163, doi:10.1016/j.epsl.2017.05.026

Bryson, J. F. J., Nichols, C. I. O., Herrero-Albillos, J., Kronast, F., Kasama, T., Alimadadi, H., van der Laan, G., Nimmo, F. & Harrison, R. J. (2015). Long-lived magnetism from solidification-driven convection on the pallasite parent body, *Nature*, *517*, 472–475, doi:10.1038/nature14114

Bryson, J. F. J., Neufeld, J. A. & Nimmo F. (2019b). Constraints on asteroid magnetic field evolution and the radii of meteorite parent bodies from thermal modelling, *Earth Planet. Sci. Lett.*, *521*, 68–78, doi:10.1016/j.epsl.2019.05.046

Bryson, J. F. J., Herrero-Albillos, J., Kronast, F., Ghidini, M., Redfern, S. A. T., van der Laan, G. & Harrison, R. J. (2014). Nanopaleomagnetism of meteoritic Fe-Ni studied using X-ray photoemission electron microscopy, *Earth Planet. Sci. Lett.*, *396*, 125–133, doi:10.1016/j.epsl.2014.04.016

Buono, A. S. & Walker, D. (2011). The Fe-rich liquidus in the Fe-FeS system from 1 bar to 10 GPa, *Geochim. Cosmochim. Acta*, *75*, 2072–2087, doi:10.1016/j.gca.2011.01.030

Carporzen, L., Weiss, B. P., Elkins-Tanton, L. T., Shuster, D. L., Ebel, D. S. & Gattacceca, J. (2011). Magnetic evidence for a partially differentiated carbonaceous chondrite parent body, *Proc. Natl. Acad. Sci.*, *108*, 6386–6389, doi:10.1073/pnas.1017165108/

Cassata, W. S., Renne, P. R. & Shuster, D. L. (2011). Argon diffusion in pyroxenes: Implications for thermochronometry and mantle degassing, *Earth Planet. Sci. Lett.*, *304*, 407–416, doi:10.1016/j.epsl.2011.02.019

Chabot, N. L., and H. Haack (2006), Evolution of asteroidal cores, in *Meteorites And The Solar System II*, edited by D. S. Lauretta and H. Y. McSween Jr, pp. 747–771, University of Arizona Press.

Denevi, B. W., Beck, A. W., Coman, E. I., Thomson, B. J., Ammannit, E., Blewett, D. T., Sunshone, J. M., De Sanctis, M.-C., Li, J.-Y., Marchi, S., Mittlefehld, D. W., Petro, N. E., Raymond, C. A. & Russell, C. T. (2016). Global variations in regolith properties on asteroid Vesta from Dawn's low-altitude mapping orbit, *Meteorit. Planet. Sci.*, *51*, 2366–2386, doi:10.1111/maps.12729

Dunlop, D. J. & Özdemir, Ö. (1997). *Rock Magnetism: Fundamentals And Frontiers*. Cambridge University Press, pp. 1-573.

Einsle, J. F., Eggeman, A. S., Martineau, B. H., Saghi, Z., Collins, S. M., Blukis, R., Bagot, P. A. J., Midgley, P. A. & Harrison R. J. (2018). Nanomagnetic properties of the meteorite cloudy zone, *Proc. Natl. Acad. Sci.*, *115*, E11436–E11445, doi:10.1073/pnas.1809378115

Elkins-Tanton, L. T., Weiss, B. P. & Zuber, M. T. (2011). Chondrites as samples of differentiated planetesimals, *Earth Planet. Sci. Lett.*, *305*, 1–10, doi:10.1016/j.epsl.2011.03.010

Fish, R. A., Goles, G. G. & Anders, E. (1960). The record in the meteorites. III. On the development of meteorites in asteroidal bodies, *Astrophys. J.*, *132*, 243–261, doi:10.1086/146918

Garrick-Bethell, I., Weiss, B. P., Shuster, D. L., Tikoo, S. M. & Tremblay, M. M. (2017). Further evidence for early lunar magnetism from troctolite 76535, *J. Geophys. Res.*, *122*, 76–93, doi:10.1002/2016JE005154

Gattacceca, J., Weiss, B. P. & Gounelle, M. (2016). New constraints on the magnetic history of the CV parent body and the solar nebula from the Kaba meteorite, *Earth Planet. Sci. Lett.*, *455*, 166–175, doi:10.1016/j.epsl.2016.09.008

Ghanbarzadeh, S., Hesse, M. A. & Prodanović, M. (2017). Percolative core formation in planetesimals enabled by hysteresis in metal connectivity, *Proc. Natl. Acad. Sci. USA*, *114*, 13406–13411, doi:10.1073/pnas.1707580114

Goldstein, J. I., Scott, E. R. D., & Chabot, N. L. (2009). Iron meteorites: Crystallization, thermal history, parent bodies, and origin, *Chemie der Erde*, *69*, 293–325, doi:10.1016/j.chemer.2009.01.002

Haack, H., Rasmussen, K. L. & Warren, P. H. (1990). Effects of regolith/megaregolith insulation on the cooling histories of differentiated asteroids, *J. Geophys. Res.*, *95*, 5111–5124, doi:10.1029/JB095iB04p05111

Harrison, R. J. & Lascu, I. (2014). FORCulator: A micromagnetic tool for simulating first-order reversal curve diagrams, *Geochem. Geophys. Geosyst.*, *15*, 4671–4691, doi:10.1002/2014GC005582

Hevey, P. J. & Sanders, I. (2006). A model for planetesimal meltdown by ^{26}Al and its implications for meteorite parent bodies, *Meteorit. Planet. Sci.*, *41*, 95–106, doi:10.1111/j.1945-5100.2006.tb00195.x

Hood, L. L. & Artemieva, N. A. (2008). Antipodal effects of lunar basin-forming impacts: Initial 3D simulations and comparisons with observations, *Icarus*, *193*, 485–502, doi:10.1016/j.icarus.2007.08.023

Hunt, A. C., Cook, D. L., Lichtenberg, T., Reger, P. M., Ek, M., Golabek, G. J. & Schönbächler, M. (2018). Late metal–silicate separation on the IAB parent asteroid: Constraints from combined W and Pt isotopes and thermal modelling, *Earth Planet. Sci. Lett.*, *482*, 490–500, doi:10.1016/j.epsl.2017.11.034

Johnson, C. L., Phillips, R. J., Purucker, M. E., et al. (2015). Low-altitude magnetic field measurements by MESSENGER reveal Mercury's ancient crustal field, *Science*, *348*, 892–895, doi:10.1126/science.aaa8720

Krot, A. N., Keil, K., Scott, E. R. D., Goodrich, C. A. & Weisberg, M. K. (2014). Classification of meteorites and their genetic relationships, in: *Treatise on Geochemistry*, H. D. Holland & K. K. Turekian, Eds., pp. 1–63

Kruijer, T. S. & Kleine, T. (2019). Age and origin of IIE iron meteorites inferred from Hf-W chronology, *Geochim. Cosmochim. Acta*, *262*, 92–103, doi:10.1016/j.gca.2019.07.039

Le Bars, M., Wieczorek, M. A., Karatekin, Ö., Cébron, D. & Laneuville, M. (2011). An impact-driven dynamo for the early Moon, *Nature*, *479*, 215–218, doi:10.1038/nature10565

Lovering, J. F. (1962). The evolution of the meteorites—evidence for the co-existence of chondritic, achondritic, and iron meteorites in a typical parent meteorite body, in: *Researches on Meteorites*, C. B. Moore, Ed., pp. 179–197

Matthes, M., Fischer-Gödde, M., Kruijer, T. S., Leya, I. & Kleine, T. (2015). Pd-Ag chronometry of iron meteorites: Correction of neutron capture-effects and application to the cooling history of differentiated protoplanets, *Geochim. Cosmochim. Acta*, *169*, 45–62, doi:10.1016/j.gca.2015.07.027

Matthes, M., van Orman, J. A. & Kleine, T. (2020). Closure temperature of the Pd-Ag system and the crystallization and cooling history of IIIAB iron meteorites, *Geochim. Cosmochim. Acta*, *285*, 193–206, doi:10.1016/j.gca.2020.07.009

Maurel, C., Weiss, B. P. & Bryson, J. F. J. (2019). Meteorite cloudy zone formation as a quantitative indicator of paleomagnetic field intensities and cooling rates on planetesimals, *Earth Planet. Sci. Lett.*, *513*, 166–175, doi:10.1016/j.epsl.2019.02.027

Maurel, C., Bryson, J. F. J., Lyons, R. J., Ball, M., Chopdekar, R. V., Scholl, A. & Weiss, B. P. (2020). Meteorite evidence for partial differentiation and protracted accretion of planetesimals, *Sci. Adv., 6*, eaba1303, doi: 10.1126/sciadv.aba1303

Neufeld, J. A., Bryson, J. F. J. & Nimmo, F. (2019). The top-down solidification of iron asteroids driving dynamo evolution, *J. Geophys. Res.*, *124*, 1331–1356, doi:10.1029/2018JE005900

Neumann, W., Breuer, D. & Spohn, T. (2014). Differentiation of Vesta: Implications for a shallow magma ocean, *Earth Planet. Sci. Lett.*, *395*, 267–280, doi:10.1016/j.epsl.2014.03.033.

Neumann, W., Henke, S., Breuer, D., Gail, P., Schwarz, W. H., Trieloff, M., Hopp, J. & Spohn, T. (2018). Modeling the evolution of the parent body of acapulcoites and lodranites: A case study for partially differentiated asteroids, *Icarus*, *311*, 146–169, doi:10.1016/j.icarus.2018.03.024

Nichols, C. I. O., Bryson, J. F. J., Herrero-Albillos, J., Kronast, F., Nimmo, F. & Harrison, R. J. (2016). Pallasite paleomagnetism: Quiescence of a core dynamo, *Earth Planet. Sci. Lett.*, *441*, 103–112, doi:10.1016/j.epsl.2016.02.037

Nichols, C. I. O. (2017). Tiny space magnets: X-ray microscopy and nanopaleomagnetism of meteoritic metal, PhD Thesis, 1–253, doi:10.17863/CAM.16820

Nichols, C. I. O., Krakow, R., Herrero-Albillos, J., Kronast, K., Northwood-Smith, G. & Harrison, R. J. (2018). Microstructural and paleomagnetic insight into the cooling history of the IAB parent body, *Geochim. Cosmochim. Acta*, *229*, 1–19, doi:10.1016/j.gca.2018.03.009

Nimmo, F. (2009). Energetics of asteroid dynamos and the role of compositional convection, *Geophys. Res. Lett.*, *36*, L10201, doi:10.1029/2009GL037997

Oran, R., Weiss, B. P. & Cohen, O. (2018). Were chondrites magnetized by the early solar wind?, *Earth Planet. Sci. Lett.*, *492*, 222–231, doi:10.1016/j.epsl.2018.02.013.

Richie, N. W. M., Newbury, D. E. & Davis, J. M. (2012). EDS measurements of X-ray intensity at WDS precision and accuracy using a silicon drift detector, *Microsc. Microanal., 18,* 892–904, doi: 10.1017/S1431927612001109

Russell, C. T., Raymond, C. A., Coradini, A., et al. (2012). Dawn at Vesta: Testing the protoplanetary paradigm, *Science*, *336*, 684–686, doi: 10.1126/science.1219381

Ruzicka, A. M. (2014). Silicate-bearing iron meteorites and their implications for the evolution of asteroidal parent bodies, *Chemie der Erde*, *74*, 3–48, doi:10.1016/j.chemer.2013.10.001

Rückriemen, T., Breuer, D. & Spohn, T. (2015). The Fe snow regime in Ganymede's core: A deep-seated dynamo below a stable snow zone, *J. Geophys. Res.*, *120*, 1095–1118, doi:10.1002/2014JE004781

Sahijpal, S. & Gupta, G. (2011). Did the carbonaceous chondrites evolve in the crustal regions of partially differentiated asteroids?, *J. Geophys. Res.*, *116*, E06004, doi:10.1029/2010JE003757

Scheinberg, A., Elkins-Tanton, L. T., Schubert, G. & Bercovici, D. (2016). Core solidification and dynamo evolution in a mantle-stripped planetesimal, *J. Geophys. Res.*, *121*, 2–20, doi:10.1002/2015JE004843

Schindelin, J., Arganda-Carreras, I., Frise, E., Kaynig, V., Longair, M., Pietzsch, T., Preibisch, S., Rueden, C., Saalfeld, S., Schmid, B., Tinevez, J.-Y., White, D. J. , Hartenstein, V., Eliceiri, K., Tomancak, P. & Cardona, A. (2012). Fiji: an open-source platform for biological-image analysis, *Nat. Methods, 9,* 676–682, doi: 10.1007/s40870-017-0094-6

Shah, J., Bates, H. C., Muxworthy, A. R., Hezel, D. C., Russell, S. S. & Genge, M. J. (2017). Long-lived magnetism on chondrite parent bodies, *Earth Planet. Sci. Lett.*, *475*, 106–118, doi:10.1016/j.epsl.2017.07.035

Stöhr, J., Wu, Y., Hermsmeier, B. D., Samant, M. G., Harp, G. R., Koranda, S., Dunham, D. & Tonner, B. P. (1993). Element-specific magnetic microscopy with circularly polarized X-rays, *Science*, *259*, 658–661, doi:10.1126/science.259.5095.658

Tarduno, J. A., Cottrell, R. D., Nimmo, F., Hopkins, J., Voronov, J., Erikson, A., Blackman, E., Scott, E. R. D., & McKinley, R. (2012). Evidence for a dynamo in the main group pallasite parent body, *Science*, *338*, 936–939, doi:10.1126/science.1225549

Tarduno, J. A., Cottrell, R. D., Watkeys, M. K., Hofmann, A., Doubrovine, P. V., Mamajek, E. E., Liu, D., Sibeck, D. G., Neukirch, L. P. & Usui, L. (2010). Geodynamo, solar wind, and magnetopause 3.4 to 3.45 billion years ago, *Science*, *327*, 1238–1240, doi:10.1126/science.1183445

Terasaki, H., D. J. Frost, D. C. Rubie, and F. Langenhorst (2008). Percolative core formation in planetesimals, *Earth Planet. Sci. Lett.*, *273*, 132–137, doi:10.1016/j.epsl.2008.06.019

Uehara, M., Gattacceca, J., Leroux, H., Jacob, D. & van der Beek, C. J. (2011). Magnetic microstructures of metal grains in equilibrated ordinary chondrites and implications for paleomagnetism of meteorites, *Earth Planet. Sci. Lett.*, *306*, 241–252, doi:10.1016/j.epsl.2011.04.008

Urey, H. C. (1959). Primary and secondary objects, *J. Geophys. Res.*, *64*, 1721–1737, doi:10.1029/JZ064i011p01721

Wang, H., Weiss, B. P., Bai, X.-N., Downey, B. G., Wang, J., Wang, J., Suavet, C., Fu, R. R. & Zucolotto, M. E. (2017). Lifetime of the solar nebula constrained by meteorite paleomagnetism, *Science*, *355*, 623–627, doi:10.1126/science.aaf5043

Wasserburg, G. J., Sanz, H. G. & Bence, A. E. (1968). Potassium-feldspar phenocrysts in the surface of Colomera, and iron meteorite, *Science*, *161*, 684–687, doi:10.1126/science.161.3842.684

Watson, G. S. (1956). A test for randomness of directions, *Geophys. J. Int.*, *7*, 160–161, doi:10.1111/j.1365-246X.1956.tb05561.x

Watson, G. S. (1983). Large sample theory of the Langevin distribution, *J. Stat. Plan. Infer.*, *8*, 245–256, doi:10.1016/0378-3758(83)90043-5

Weiss, B. P. & Elkins-Tanton, L. T. (2013). Differentiated planetesimals and the parent bodies of chondrites, *Annu. Rev. Earth Planet. Sci.*, *41*, 529–560, doi:10.1146/annurev-earth-040610-133520

Weiss, B. P., Vali, H., Baudenbacher, F. J., Kirschvink, J. L., Stewart, S. T. & Shuster, D. L. (2002). Records of an ancient Martian magnetic field in ALH84001, *Earth Planet. Sci. Lett.*, *201*, 449–463, doi:10.1016/S0012-821X(02)00728-8

Weiss, B. P., Gattacceca, J., Stanley, S., Rochette, P. & Christensen, U. R. (2010). Paleomagnetic records of meteorites and early planetesimal differentiation, *Space Sci. Rev.*, *152*, 341–390, doi:10.1007/s11214-009-9580-z

Weiss, B. P., Berdahl, J. S., Elkins-Tanton, L. T., Stanley; S., Lima, E. A. & Carporzen, L. (2008). Magnetism on the angrite parent body and the early differentiation of planetesimals, *Science*, *322*, 713–716, doi:10.1126/science.1162459

Williams, Q. (2009). Bottom-up versus top-down solidification of the cores of small solar system bodies: Constraints on paradoxical cores, *Earth Planet. Sci. Lett.*, *284*, 564–569, doi:10.1016/j.epsl.2009.05.019

Worsham, E. A., Bermingham, K. R., & Walker, R. J. (2017). Characterizing cosmochemical materials with genetic affinities to the Earth: Genetic and chronological diversity within the IAB iron meteorite complex, *Earth Planet. Sci. Lett.*, *467*, 157–166, doi:10.1016/j.epsl.2017.02.044

Yang, C. W., Williams, D. A. & Goldstein, J. I. (1996). A revision of the Fe-Ni phase diagram at low temperatures (< 400°C), *J. Phase Equilib.*, *17*, 522–531

Yeem, S. & Harrison, R. J. (2019). Interaction-driven domain-state transition in the meteorite cloudy zone: a hybrid micromagnetic approach to modelling remanence acquisition, abstract GP23B–0789, *100th AGU Fall Meeting*, San Francisco, CA